C. T.-C. Nguyen and R. T. Howe, “Design and performance of monolithic CMOS micromechanical resonator oscillators,” Proceedings, 1994 IEEE International Frequency Control Symposium, Boston, MA, May 31-June 3, 1994, pp. 127-134.

DESIGN AND PERFORMANCE OF CMOS MICROMECHANICAL RESONATOR OSCILLATORS

Clark T.-C. Nguyen and Roger T. Howe

Berkeley Sensor & Actuator Center
Department of Electrical Engineering and Computer Sciences
and the Electronics Research Laboratory
University of California at Berkeley
Berkeley, California 94720

Abstract

A completely monolithic high-Q oscillator, fabricated via a combined CMOS plus surface micromachining technology, is described, for which the oscillation frequency is controlled by a polysilicon micromechanical resonator to achieve high stability. It is shown that the closed-loop, steady-state oscillation amplitude of this oscillator can be controlled through the dc-bias voltage applied to the capacitively driven and sensed μresonator. Brownian motion and mass loading phenomena are shown to have a greater influence on short-term stability in this micro-scale.

Introduction

Crystal oscillators are widely used to generate precision frequency standards for complex integrated circuits. With the current trend to include increasing amounts of a total system on a single silicon chip, designers have begun to include the oscillator function, without the crystal, on the silicon die. A fully monolithic high-Q oscillator, which includes the “crystal” element as well as sustaining CMOS electronics on-chip, is thus desirable.

Such an oscillator has recently been demonstrated [1], which utilizes a surface-micromachined, polycrystalline silicon resonator [2] frequency-setting element and CMOS electronics to sustain oscillation, all fabricated onto a single silicon chip (Fig. 1). The cross-section of the combined CMOS plus surface micromachining technology used to fabricate this oscillator [1,3] is shown in Fig. 2.

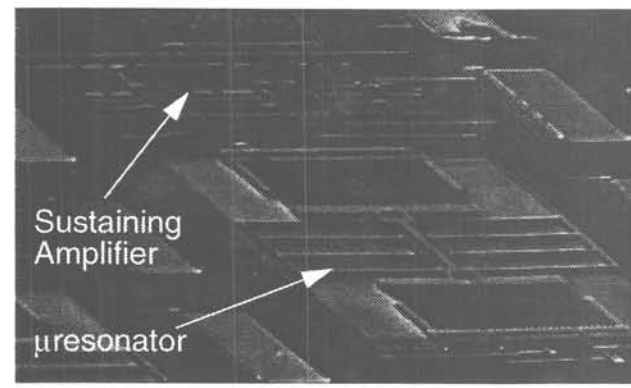

Fig. 1: SEM of the integrated CMOS μresonator oscillator.

With Q's of over 80,000 [4] under vacuum and center frequency temperature coefficients in the range of -10 ppm/°C (several times less with nulling techniques) [5], polysilicon micromechanical resonators can serve reasonably well as miniaturized substitutes for crystals in a variety of high-Q oscillator and filtering applications. As the high-Q element is miniaturized, however, such phenomena as Brownian motion and mass loading noise [6] begin to have greater influence on oscillator short-term stability and may limit the ultimate stability of micro-scale resonators unless design strategies which minimize these effects are implemented. After an initial focus on resonator transducer and oscillator design, this paper will address some of these performance limiting effects.

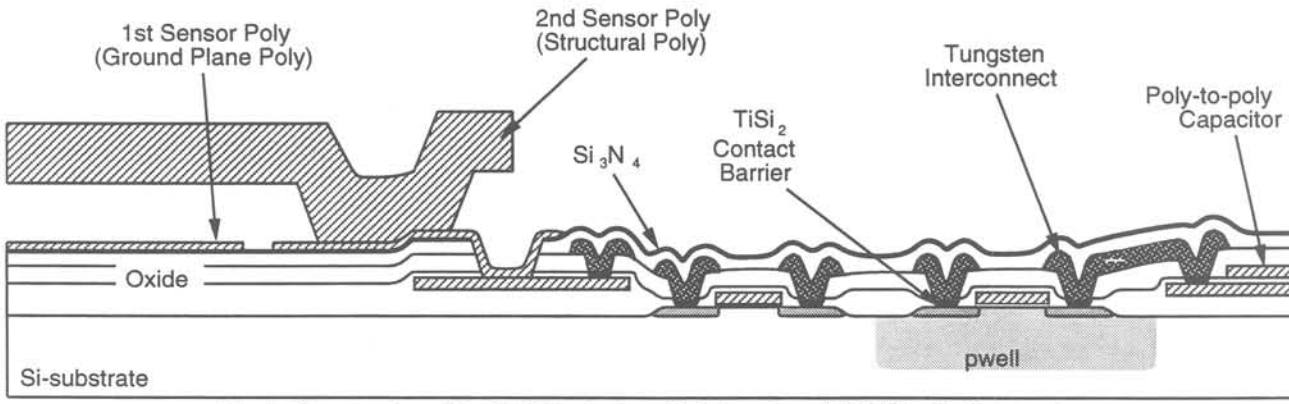

Fig. 2: Cross-section of the MICS technology for integration of CMOS and microstructures.

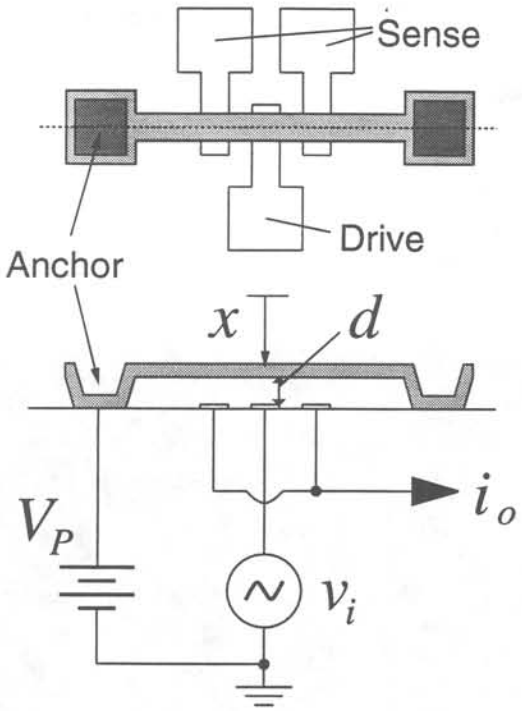

Fig. 3: Overhead and cross-sectional view of a vertical parallel-plate capacitively driven resonator with typical applied bias and excitation voltages.

Resonator Design

To simplify the task of integrating CMOS with micromechanics, capacitive excitation and detection is utilized for the μresonators in this work. A variety of capacitive topologies are available in this technology, and each will dictate the frequency tuning range and stability of the μresonator.

Figure 3 shows the cross-section of a parallel-plate capacitively driven μcantilever resonator in a typical bias and excitation configuration. [7]. Here, an ac voltage v_i electrostatically drives the cantilever. The dc-bias voltage V_P amplifies the resulting force components at the frequency of v_i. In this scheme, the beam-to-electrode capacitance is nonlinearly dependent upon beam displacement, and thus, the change in capacitance vs. displacement, $\partial C/\partial x$, is a strong function of displacement:

$$\frac{\partial C}{\partial x} = \frac{C_o}{d}\left(1-\frac{x}{d}\right)^2 , \qquad (1)$$

where C_o is the static beam-to-electrode capacitance. Using (1), the components of force f_d at the input frequency acting on the beam of Fig. 3 are

$$f_d\big|_{\omega_o} = \frac{1}{2}(V_P - v_i)^2 \frac{\partial C}{\partial x}\bigg|_{\omega_o} = -V_P\frac{C_o}{d}v_i + V_P^2\frac{C_o}{d^2}x \ . \qquad (2)$$

The second term of (2) implies an electrical spring constant, $k_e=V_P^2(C_o/d^2)$, which adds to the mechanical spring constant k_m and makes the center frequency f'_o a function of the dc-bias voltage V_P:

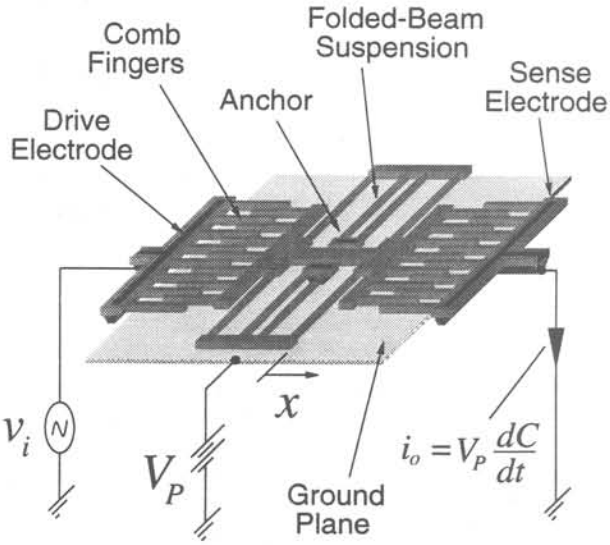

Fig. 4: Perspective view of a two-port, folded-beam, lateral comb-driven resonator with typical applied bias and excitation voltages. All areas of the resonator and electrodes are suspended 2 μm above the substrate, except for the darkly shaded areas, which are the anchor points.

$$f'_o = f_o\left(1-\frac{V_P^2 C_o}{k_m d^2}\right)^{1/2} . \qquad (3)$$

The above provides a convenient means for voltage control of the center frequency, making parallel-plate driven resonators useful for VCO applications. A -3600 ppm/V fractional frequency change is typical for a 20 kHz μresonator with a nominal V_P=10 V. However, (3) also suggests that oscillators referenced to parallel-plate capacitively driven μresonators are less stable against power supply variations, due to electronic noise or temperature. If V_P=10 V is supplied by a Zener diode reference, which typically varies 250 mV over a 0°-100°C range, the corresponding fractional frequency variation for a 20 kHz μresonator is 864 ppm over this temperature range. If a bandgap reference is used (3 mV variation over a 0°-100°C range), the $\Delta f/f_o$ variation is 10 ppm.

To eliminate this component of frequency instability, the electrode-to-resonator capacitance must be made to vary linearly with resonator displacement. In this work, this is achieved by using interdigitated-comb finger drive and sense capacitors [2]. Figure 4 shows a μresonator which utilizes interdigitated-comb finger transduction in a typical bias and excitation configuration. The μresonator consists of a shuttle mass, with fingers on opposite sides, suspended 2 μm above the substrate by folded flexures, which are anchored to the substrate at two central points. The shuttle mass is free to move in the direction indicated, parallel to the plane of the silicon substrate. Folding the suspending beams as shown provides two main advantages: first, post-

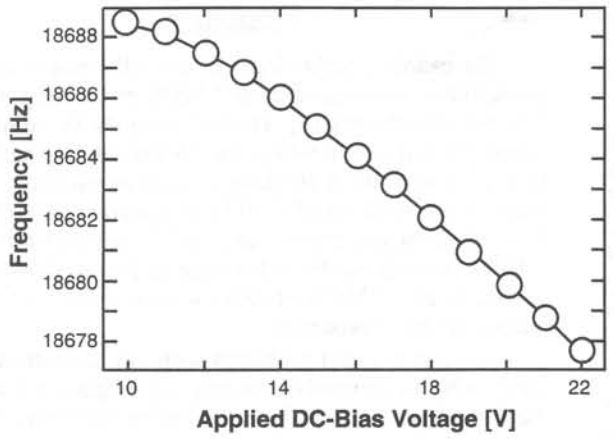

Fig. 5: Plot of center frequency vs. dc-bias voltage V_P for a comb-driven μresonator.

fabrication residual stress is relieved if all beams expand or contract by the same amount; and second, spring stiffening nonlinearity in the suspension is reduced, since the folding truss is free to move in a direction perpendicular to the resonator motion.

The drive and sense capacitors consist of overlap capacitance between the interdigitated shuttle and electrode fingers. As the shuttle moves, these capacitors vary linearly with displacement. Thus, $\partial C/\partial x$ is a constant, making the drive force f_d at the input frequency independent of x:

$$f_d\big|_{\omega_o} = V_P \frac{\partial C}{\partial x} v_i \,. \tag{4}$$

The electrical spring constant k_e is, thus, ideally nonexistent, and the resonator center frequency is independent of V_P.

For actual comb-driven μresonators, nonidealities do not permit absolute cancellation of k_e, and some variation of frequency with V_P is observed. Figure 5 shows a plot of center frequency vs. dc-bias for a micromachined comb-driven resonator. The frequency variation is about -54 ppm/V , corresponding to 14 ppm and 0.2 ppm fractional frequency variations over a 0°-100°C range for a Zener diode and a bandgap reference, respectively.

Oscillator Design

The equivalent circuit for the two-port μmechanical resonator of Fig. 4, shown transformed to an equivalent LCR representation, is presented in Fig. 6 [7,8]. Due to the use of weak capacitive electromechanical transduction, the motional element values are quite different from those for quartz crystal units (which typically have R_x=50Ω, C_x=0.04 pF, L_x=0.25 H), and this dictates differing strategies in the design of μresonator oscillators versus macroscopic crystal oscillators. The detailed, transistor-level circuit design and operation of this oscillator has already been discussed elsewhere [1]. The focus of the present discussion centers on issues of amplitude limiting.

Figure 7 shows a system-level schematic describing the basic architecture used for this oscillator. Since the

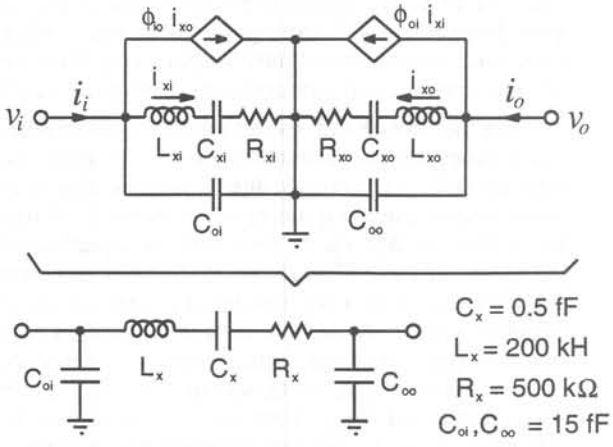

$$R_{xn} = \sqrt{km}\left[Q V_P^2 (\partial C/\partial x)_n^2\right]^{-1} \qquad C_{xn} = k^{-1} V_P^2 (\partial C/\partial x)_n^2$$

$$L_{xn} = m\left[V_P^2 (\partial C/\partial x)_n^2\right]^{-1} \qquad \phi_{mn} = \frac{(\partial C/\partial x)_m}{(\partial C/\partial x)_n}$$

Fig. 6: Equivalent circuit for a two-port μresonator showing the transformation to the more convenient LCR form. In the equations, k is the system spring constant and $(\partial C/\partial x)_n$ is the change in capacitance per displacement at port n of the μresonator.

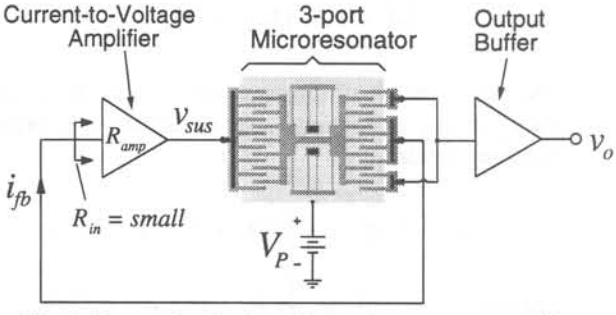

Fig. 7: System level schematic for the μresonator oscillator.

motional resistance of the μresonator is large (Fig. 6), a series resonant oscillator architecture is utilized to minimize Q-loading [1]. As shown, the system consists of a three-port micromechanical resonator, for which two ports are embedded in a positive feedback loop with a sustaining transresistance amplifier, while a third port is directed to an output buffer. The use of a third port effectively isolates the sustaining feedback loop from variations in output loading. Conceptually, the sustaining amplifier and μmechanical resonator comprise negative and positive resistances, respectively. During start-up, the negative resistance of the amplifier R_{amp} is larger in magnitude than the positive resistance of the resonator R_x, and oscillation results. Oscillation builds up until either some form of nonlinearity or a designed automatic-level control circuit alters either or both resistors so that, R_{amp}=R_x, at which point the oscillation amplitude limits.

For oscillators controlled by quartz crystals, the nonlinearity usually appears in the sustaining circuit, where transistors enter the triode region at large voltage amplitudes,

reducing effective device transconductances until the loop gain drops to unity. Limiting due to crystal nonlinearity is rare, since quartz crystal units display very little nonlinearity over normal oscillator operating voltage ranges [9].

On the other hand, even though comb-driven, folded-beam μmechanical resonators are only slightly less linear than crystals [1], limiting due to nonlinearity in flexural-mode μresonators is quite practical through adjustment of the dc-bias voltage V_P. As seen from the equations of Fig. 6, the values of the motional circuit elements representing the capacitively driven μmechanical resonator are strongly dependent upon the dc-bias voltage V_P applied to the resonator. In particular, the value of motional resistance R_x is inversely proportional to the square of V_P, and thus, it can be set to just under R_{amp} at the start of oscillation by proper selection of V_P. As oscillation builds up, stiffening nonlinearities in the resonator springs then increase the effective R_x of the μresonator until R_x=R_{amp}, when the loop gain equals one and the amplitude limits. The steady-state amplitude of oscillation is thus a function of the initial separation between R_x and R_{amp}, which is in turn a function of V_P.

To quantify this limiting process, we first write an expression describing the spring nonlinearity. Since at resonance, the force is amplified by the Q, we have

$$Qf = k_1 x + k_2 x^2 + k_3 x^3 + \ldots , \tag{5}$$

where k_1 is the small displacement system spring constant, and k_2 and k_3 model the spring nonlinearity. A series reversion then yields

$$x = b_1 Qf + b_2 (Qf)^2 + b_3 (Qf)^3 + \ldots , \tag{6}$$

where $b_1 = k_1^{-1}$, $b_2 = -k_2 k_1^{-3}$, and $b_3 = 2k_2^2 k_1^{-5} - k_3 k_1^{-4}$. Retaining only those components at resonance, the phasor form for displacement X is then given by

$$X = b_1 QF + \frac{3}{4} b_3 Q^3 F^3 . \tag{7}$$

Inserting expressions for current I_x as a function of X and force F in terms of input voltage V_i into (7) [8], assuming a Duffing nonlinearity in the resonator springs (k_2=0), and differentiating, we have

$$\frac{\partial I_x}{\partial V_i} = \frac{Q}{k_1}\omega_o V_P^2 \left(\frac{\partial C}{\partial x}\right)^2 - \frac{9}{4}\frac{k_3 Q^3}{k_1^4}\omega_o V_P^4 \left(\frac{\partial C}{\partial x}\right)^4 V_i^2 = \frac{1}{R_{ss}} \tag{8}$$

Equation (8) shows that as the amplitude of oscillation V_i grows, the small-signal series resistance R_{ss} increases until it equals the transresistance of the sustaining amplifier, R_{amp}, at which point the loop gain is unity, and V_i settles at a steady-state value. From (8), the steady-state V_i is clearly controllable through the resonator dc-bias voltage V_P.

Fabrication

The enabling technology for the fully monolithic high-Q oscillator combines planar CMOS processing with surface micromachining [3]. The technologies are combined in a modular fashion, in which the CMOS processing and surface micromachining are done in separate process modules, with no intermixing of CMOS or micromachining steps. This Modular Integration of CMOS and microStructures (MICS) process has the advantage in that it allows the use of nearly any CMOS process with a variety of surface micromachining processes.

In order to avoid problems with microstructure topography, which commonly includes step heights of 2 to 3 μm, the CMOS module is fabricated before the microstructure module. Although this solves topography problems, it introduces constraints on the CMOS. Specifically, the metallization and contacts for the electronics must be able to survive post-CMOS micromachining processing with temperatures up to 835°C. Aluminum interconnect, the industry standard, cannot survive these temperatures. For this reason, tungsten with $TiSi_2$ contact barriers is used as interconnect for this process.

A cross-sectional outline of the MICS process sequence is presented in Fig. 8. The fabrication process begins with standard CMOS up to and including the contact cut for the first metallization (Fig. 8(a)). At this point, a thin film of titanium is sputter deposited onto the wafer surface, and then rapid-thermal annealed (RTA) for 30 seconds at 600°C in a nitrogen ambient to form $TiSi_2$ at points where titanium contacts silicon. Unreacted titanium is then etched away using a 3:1 NH_4OH:H_2O_2 solution, and another RTA is performed for 10 seconds at 1000°C. At this point, the cross-section appears as in Fig. 8(b). A 6000 Å film of tungsten is then sputter deposited and patterned to form the single-level interconnect (Fig. 8(c)). Subsequent low-pressure chemical vapor depositions (LPCVD) of 5000 Å of low-temperature oxide (LTO) and 1500 Å of silicon-rich nitride, at 450°C and 835°C, respectively, serve to passivate the metal (Fig. 8(d)).

Vias are then plasma etched through the nitride and underlying oxide to expose gate polysilicon runners that were formed during CMOS processing (Fig. 8(e)). These runners serve as an intermediate conductive level that joins the CMOS tungsten interconnect with the structural polysilicon interconnect. Direct contact between the first structural (ground plane) polysilicon and tungsten metal never occurs. This originally was a precaution to prevent contamination of the polysilicon deposition system by tungsten.

Next, 3000 Å of *in situ* phosphorous-doped LPCVD polysilicon is deposited at 610°C and patterned to define the interconnect and ground plane polysilicon for the microstructures (Fig. 8(f)). This is followed by a 2 μm LPCVD deposition (450°C) of phosphosilicate glass (PSG) that serves as a sacrificial layer to be removed when releasing the mechanical structures. Next, a contact cut in the PSG defines the anchor points for resonators and electrodes (Fig. 8(g)), and 2 μm of *in situ* phosphorous-doped LPCVD

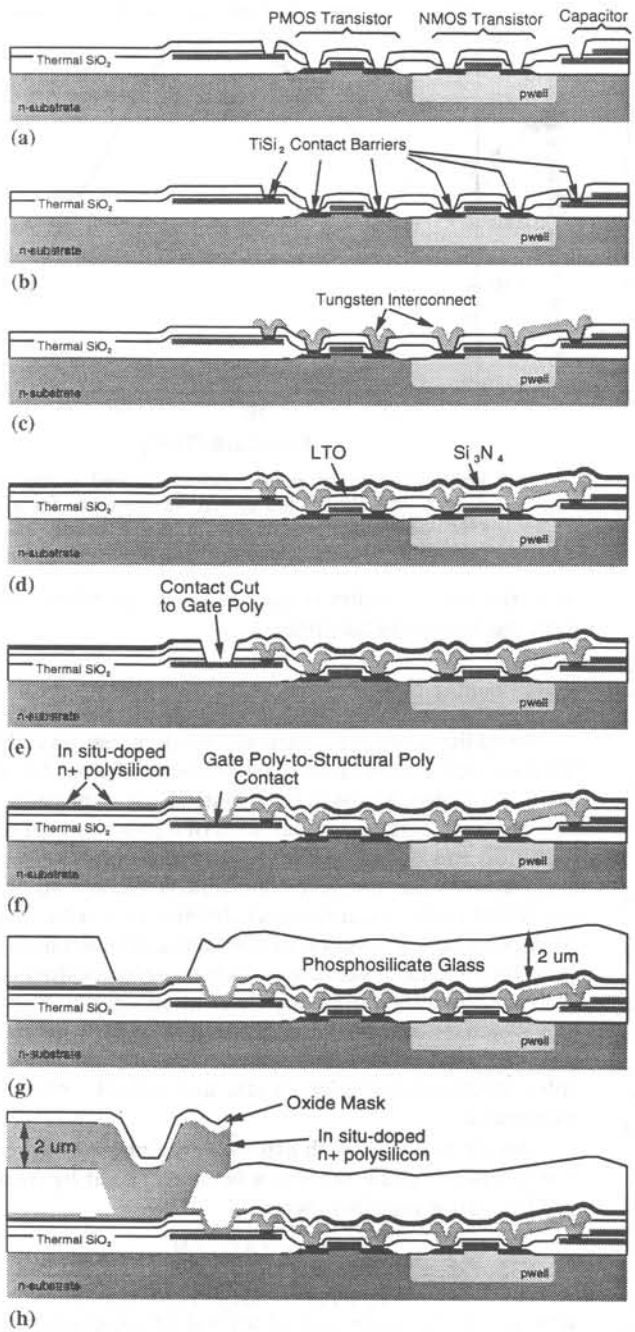

Fig. 8: Cross-sectional process flow for the CMOS plus microstructures fabrication technology. (a)-(c) constitute the metallization steps; (d)-(f) present the circuit-to-structure interface; and (g)-(h) show the micromachining steps. The final cross-section is presented Fig. 1.

polysilicon is deposited at 610°C to serve as the structural material.

The structural material is then capped with a 5000 Å film of LTO, which deposits conformally onto the polysilicon. A thin layer of photoresist is applied and patterned with a single mask that defines resonator geometries, including

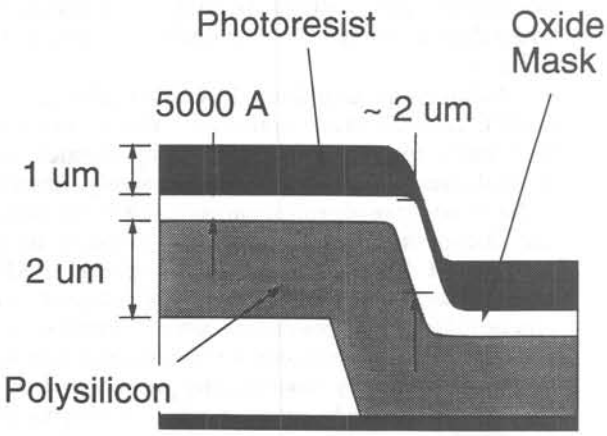

Fig. 9: Cross-section illustrating how a conformal oxide mask can reduce photoresist thickness requirements over large steps, thus, enhancing lithographic resolution. The oxide is much thicker vertically in the regions where photoresist is thin.

interdigitated-comb fingers. The oxide cap is first plasma etched using a CF_4/C_2F_6-based chemistry, which is very selective towards oxide, but which etches silicon very slowly. The oxide then serves as a hard mask for the ensuing plasma etch that patterns the structural polysilicon. This etch is done using a Cl_2-based chemistry that attacks silicon, but etches oxide very slowly. At this point, the structural polysilicon is fully patterned, and the cross-section of Fig. 8(h) results.

Use of this oxide mask greatly enhances the resolution with which finger gaps may be defined. Without the oxide mask, a double or triple layer of photoresist would be required to insure proper coverage of large steps, which occur around the anchors of the resonators and electrodes. With an oxide mask, however, the photoresist is no longer required to cover large steps, since now oxide protects the underlying polysilicon. During the oxide mask etch, the oxide along the step slopes may be attacked, since the photoresist is very thin along the steep slopes. However, as illustrated in Fig. 9, the vertical thickness of the conformal oxide layer is much larger along the these slopes, so oxide will remain to protect polysilicon even after long anisotropic overetches during oxide mask patterning. Thus, a much thinner film of photoresist may be used when an oxide mask is present, which leads to improved lithographic resolution. High resolution is extremely important for oscillator or signal processing applications of capacitively transduced resonators, since the degree of electromechanical coupling achievable via capacitive transduction is directly related to the gap spacings between interdigitated fingers.

Continuing with the process flow, a stress anneal is performed via RTA for 1 minute at 950°C, followed by a sequence of etches to expose the conductive backside of the silicon wafer. Finally, the wafer is dipped in 5:1 buffered hydrofluoric acid to remove the sacrificial PSG and free the microstructures. The wafers are dried using a supercritical carbon dioxide technique, which prevents sticking of the

structures to the substrate by eliminating surface tension forces during drying [13]. The final cross-section is shown in Fig. 1.

Although quite different from the traditional 1 hour at 1050°C furnace stress anneal [2], which cannot be used here due to the presence of CMOS electronics, the rapid thermal stress anneal performs comparably. However, due to the heavy phosphorous concentration in the polycrystalline silicon, the residual compressive stress in the polysilicon films of this work is still quite large and is difficult to anneal away. Thus, stress-relaxing designs, such as cantilevers or folded-beam resonators, are required for the current process. The aforementioned stress problems may be alleviated in the future by lowering the phosphorous content in the μresonators, or by using *in situ* boron-doped polysilicon. The latter solution has the additional advantage of substantially reducing the polysilicon deposition rate.

Short-term Frequency Stability

Superposed Electronic Noise

The phase noise power due to superposed electronic noise from the sustaining amplifier may be predicted theoretically using a procedure similar to that in [10]. Assuming a linear oscillator, and thus, neglecting $1/f$ mixed noise, the equation for the relative oscillator phase noise density N_{op} to carrier C power ratio at a deviation f_m from carrier frequency f_o is

$$\left.\frac{N_{op}}{C}\right|_{\delta f = f_m} = \frac{\left(\overline{i_a^2}/\Delta f\right)R_{amp}^2}{R_L R_{in} C}\frac{1}{8Q^2}\left(\frac{f_o}{f_m}\right)^2. \qquad (9)$$

where R_{in} and R_L are the input and load resistances, respectively.

For the case of an oscillator utilizing a micro-scale resonator, the noise current power $\overline{i_a^2}$ above must include both contributions from the amplifier and from Brownian motion of the miniaturized resonator. Using the thermal equilibrium arguments of [11], the Brownian noise displacement at resonance is given by

$$\frac{\overline{x_n^2}}{\Delta f} = \frac{4Q\sqrt{m}k_B T}{k^{3/2}} \propto \sqrt{m}\,, \qquad (10)$$

where k is the (small displacement) spring constant, k_B is the Boltzmann constant, and T is temperature. Equation (10) predicts that as a resonator is further miniaturized, the noise displacement power due to Brownian motion will decrease, which at first glance would seem to improve noise performance. However, capacitive transduction detects the velocity of the resonator, not its displacement. Thus, the output current i_x of the μresonator corresponds to velocity, and the effective noise current due to Brownian motion is given by

$$\frac{\overline{i_x^2}}{\Delta f} = \frac{4k_B T}{R_x} \propto \frac{1}{\sqrt{m}}\,, \qquad (11)$$

which increases as resonator size decreases. For the oscillator design of this work, the electronic noise contribution from Brownian motion is usually equal to or less than that from the sustaining amplifier.

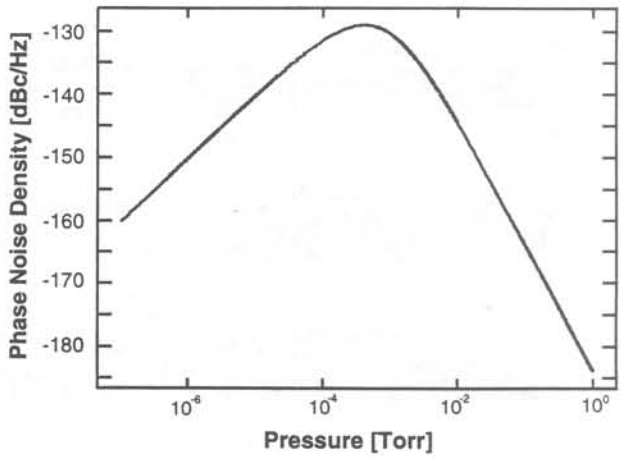

Fig. 10: Predicted plot of mass loading-derived phase noise density 100 Hz off the carrier vs. pressure for a 14.4 kHz μresonator oscillator in an ambient of gas molecules with the molecular weight of nitrogen.

Mass Loading Noise

In addition to superposed electronic noise, any physical phenomenon which causes instantaneous frequency deviations in the resonator will contribute to the total phase noise power. Given that the typical mass of a μmechanical resonator is on the order of 10^{-11} kg, mass loading noise is expected to make a sizable contribution. Mass loading noise [6] arises from instantaneous differences in the rates of adsorption and desorption of contaminant molecules to and from the resonator surface, which cause mass fluctuations, and consequently, frequency fluctuations. Some of the factors which determine the magnitude of mass loading noise include the adsorption/desorption rate of contaminant molecules, contaminant molecule size and weight, pressure, and temperature.

An expression which estimates the phase noise density due to mass loading noise has been proposed by Yong and Vig [6], and is repeated, here:

$$S_\phi(f) = \frac{8r_o r_1 (\Delta f)^2 / N}{(r_o + r_1)^3 + 4\pi^2 f^2 (r_o + r_1)} \cdot \frac{1}{f^2}\,, \qquad (12)$$

where r_o is the mean rate of arrival of contaminant molecules at a resonator site, r_i is the desorption rate of molecules from the surface, and N is the total number of sites on the resonator surface at which adsorption or desorption can occur. Equation (12) assumes a sticking probability of one if an adsorption site is uncontaminated and zero if contaminated, so the magnitude of phase noise predicted will be higher or lower than the actual value, depending upon the actual sticking probabilities for the molecules involved. The qualitative trends predicted by (12), however, are useful.

Using (12) and accounting for the pressure dependence of r_o [6], the phase noise density due to mass loading for the 14.4 kHz μresonator of Fig. 1 can be plotted as a function of

pressure. Figure 10 presents such a plot for phase noise at a 100 Hz deviation from the carrier, where a contaminant molecule with the molecular weight of nitrogen has been assumed. The desorption energy was assumed to be 12 kcal/mol. The mass loading-derived phase noise density is largest at an intermediate value of pressure and smallest at the higher and lower pressures. At the peak (around 0.5 mTorr), the predicted phase noise density is -130 dBc/Hz, which is higher than that predicted for macroscopic quartz resonators of comparable frequency.

As the μresonator frequency increases, its mass generally decreases, and the phase noise contribution from mass loading is expected to become even more significant. The mass of a 10.7 MHz tuning fork μresonator is on the order of only 10^{-12} kg, and for this design the predicted phase noise density due to mass loading at the peak of the pressure curve is −105 dBc/Hz for 100 Hz deviation from the carrier and −142 dBc/Hz for 5 kHz deviation from the carrier.

For μmechanical resonators with Q's in the range of 50,000 to 500,000, viscous gas damping [12] ceases to be the dominant energy dissipation mechanism at pressures in the range of 0.1 to 1 mTorr, where intrinsic material damping mechanisms become dominant, and the Q of the resonator is maximized. As seen from Fig. 10, the phase noise density due to mass loading may still be large at this pressure value, and even lower pressures are required to alleviate this noise source. Thus, by setting an upper limit on operation pressure given a required phase noise density level, mass loading phenomena may ultimately dictate the design of μmechanical resonator oscillators.

On-chip vacuum encapsulation techniques have been previously investigated which provide vacuums with pressures below 300 mTorr [16], or perhaps better [14,15]. Encapsulation strategies which use gettering elements to remove residual gases may potentially provide the even lower pressure ranges (10^{-7} to 10^{-6} Torr) requested by Fig. 10.

Experimental Results

The fabricated oscillator was bonded up in a dual-in-line package and tested under a variable pressure vacuum probe station. Figure 11 shows a typical oscilloscope plot for a 16.5 kHz version of this oscillator. The amplitude of oscillation was visibly controllable through adjustment of V_P, consistent with the discussion of Section III. A measured plot of steady-state oscillator output voltage versus μresonator dc-bias is presented in Fig. 12. Over most of the range of V_P, the oscillation was visibly and measurably clean. However, over about a 5 V range some chaotic behavior of the resonator was visible under microscope. This indicates that in a finite range of dc-bias voltage, the oscillator may be exhibiting second-order nonautonomous behavior when limiting through resonator nonlinearity [17]. This phenomenon is currently under investigation.

In addition, accurate measurements of the phase noise of this oscillator are in progress.

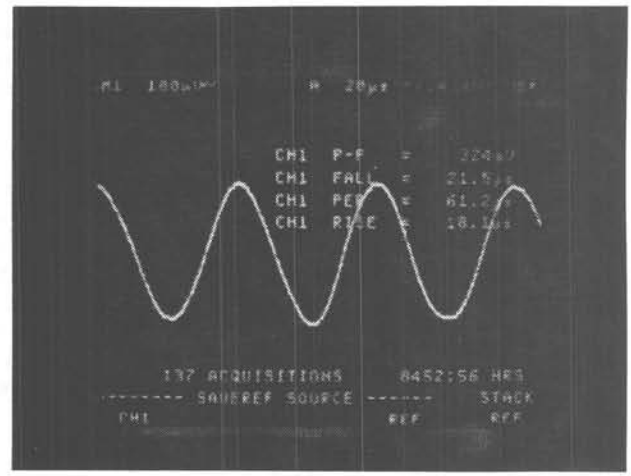

Fig. 11:Oscilloscope waveform for a μresonator oscillator.

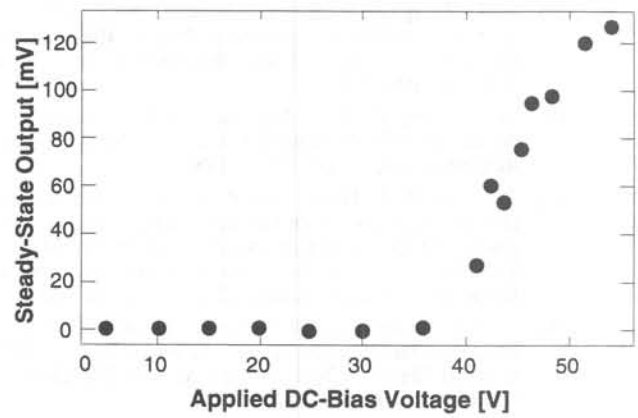

Fig. 12:Measured dependence of oscillator steady-state voltage output amplitude as a function of μresonator dc-bias.

Conclusions

Completely monolithic, highly stable, high-Q oscillators utilizing surface-micromachined polysilicon mechanical resonators have been designed, fabricated, and tested with particular attention to amplitude control and phase noise performance. Due to the novelty of the process and the devices, conservative measures were taken for the designs, and oscillators up to only 100 kHz were fabricated. Designs up to a few megaHertz are feasible using folded-beam resonator designs, and higher frequencies (tens of MHz) should be feasible using more advanced designs aimed at maximizing resonator quality factor, which may otherwise degrade with increasing frequency. Both material and architectural improvements should be possible to increase μresonator Q.

The consequences associated with miniaturization of high-Q elements were addressed via this oscillator. Brownian motion and mass loading were identified as phenomena which become increasingly important contributors to phase noise as resonator dimensions shrink. According to theory, mass loading-induced phase noise can be substantially

reduced by operating the miniature μmechanical resonator under very low pressures. For this reason, integrated vacuum encapsulation techniques may play an important role in the future.

Acknowledgements. The authors would like to thank Shenqing Fang for assistance in CMOS fabrication, as well as Katalin Voros and the staff of the Berkeley Microfabrication Laboratory for process support. In addition, we are grateful for discussions with John Vig of the U.S. Army Electronics Technology and Devices Laboratory, whose insights on mass loading contributed much to this work. This research was supported by the Berkeley Sensor & Actuator Center (BSAC).

References

[1] C. T.-C. Nguyen and R. T. Howe, "CMOS micromechanical resonator oscillator," *Technical Digest*, IEEE International Electron Devices Meeting, Washington, D.C., Dec. 5-8, 1993, pp. 199-202.

[2] W. C. Tang, C. T.-C. Nguyen, and R. T. Howe, "Laterally driven polysilicon resonant microstructures," *Sensors and Actuators,* vol. 20, pp. 25-32, 1989.

[3] W. Yun, R. T. Howe, and P. R. Gray, "Surface micromachined, digitally force-balanced accelerometer with integrated CMOS detection circuitry, *Technical Digest,* IEEE Solid-State Sensor & Actuator Workshop, Hilton Head Island, South Carolina, June 22-25, 1992, pp. 126-131.

[4] C. T.-C. Nguyen and R. T. Howe, "Quality factor control for micromechanical resonators," *Technical Digest*, IEEE International Electron Devices Meeting, San Francisco, California, Dec. 13-16, 1992, pp. 505-508.

[5] C. T.-C. Nguyen and R. T. Howe, "Microresonator frequency control and stabilization using an integrated micro oven," *Technical Digest,* 7th International Conference on Solid-State Sensors and Actuators (Transducers'93), Yokohama, Japan, June 1993, pp. 1040-1043.

[6] Y. K. Yong and J. R. Vig, "Resonator surface contamination—a cause of frequency fluctuations?" *IEEE Trans. Ultrason. Ferroelec. Freq. Contr.*, vol. 36, no. 4, pp. 452-458, March 1989.

[7] R. T. Howe and R. S. Muller, "Resonant microbridge vapor sensor," *IEEE Trans. Electron Devices*, vol. ED-33, pp. 499-506, 1986.

[8] C. T.-C. Nguyen, "Electromechanical characterization of microresonators for circuit applications," M.S. Report, Dept. of Electrical Engineering and Computer Sciences, University of California at Berkeley, April 1991.

[9] F. L. Walls and J.-J. Gagnepain, "Environmental sensitivities of quartz oscillators," *IEEE Trans. Ultrason. Ferroelec. Freq. Contr.*, vol. 39, no. 2, pp. 241-249, March 1992.

[10] W. P. Robins, *Phase Noise in Signal Sources*. London: Peter Peregrinus Ltd., 1982.

[11] T. B. Gabrielson, "Mechanical-thermal noise in micromachined acoustic and vibration sensors, *IEEE Trans. Electron Devices*, vol. 4, no. 5, pp. 903-909, May 1993.

[12] R. A. Buser, "Theoretical and experimental investigations of silicon single crystal resonant structures," Ph.D. Thesis, Inst. of Microtechnology, University of Neuchatel, CH-2000 Neuchatel, Switzerland, July 1989.

[13] G. T. Mulhern, D. S. Soane, and R. T. Howe, "Supercritical carbon dioxide drying of microstructures," 7th International Conference on Solid-State Sensors and Actuators (Transducers'93), Yokohama, Japan, June 1993, pp. 296-299.

[14] H. Guckel, *et al*, "The application of fine-grained tensile polysilicon to mechanically resonant transducers," *Sensors and Actuators*, **A21-23**, pp. 346-351 (1990).

[15] H. Guckel, *et al*, "Polysilicon resonant microbeam technology for high performance sensor applications," *Technical Digest,* IEEE Solid-State Sensor & Actuator Workshop, Hilton Head Island, South Carolina, June 22-25, 1992., pp. 153-156.

[16] L. lin, *et al*, "Vacuum-encapsulated lateral microresonators," *Technical Digest,* 7th International Conference on Solid-State Sensors and Actuators (Transducers'93), Yokohama, Japan, June 1993, pp. 270-273.

[17] T. S. Parker and L. O. Chua, "Chaos: a tutorial for engineers," *Proceedings of the IEEE,* vol. 75, no. 8, pp. 982-1008.